Structural, magnetic, and transport properties of Co nanoparticles within a Cu matrix

Júlio C. Cezar

LNLS - Laboratório Nacional de Luz Síncrotron, CP 6192, 13084-971, Campinas, Brazil
and Instituto de Física Gleb Wataghin–Unicamp, CP 6165, 13083-970, Campinas, Brazil

Hélio C. N. Tolentino*

LNLS - Laboratório Nacional de Luz Síncrotron, CP 6192, 13084-971, Campinas, Brazil

Marcelo Knobel

Instituto de Física Gleb Wataghin–Unicamp, CP 6165, 13083-970, Campinas, Brazil

(Received 15 October 2002; revised manuscript received 21 January 2003; published 5 August 2003)

We have studied the structural, magnetic, and transport properties of Co nanoparticles embedded in a Cu matrix using x-ray absorption fine structure (XAFS) spectroscopy, macroscopic magnetization, and transport measurements. We observed by XAFS, on annealed samples containing 3, 10, 12, and 25 at. % Co, that there is a systematic contraction of the average coordination distance around Co atoms with the increasing Co content and annealing. The results are consistent with the growing of small fcc nanoparticles and correlated to the evolution in the superparamagnetic behavior, observed by magnetization measurements. We present a simple model to connect the diameter of Co nanoparticles to the average coordination distance and its mean-square fluctuation. Our analysis leads to cluster sizes ranging from 1 nm to more than 8 nm. We found that for a particle diameter of about 4.4 nm the sample containing 10 at. % Co presents a maximum in the giant magnetoresistance (GMR). Moreover, we observed that the disorder is significantly reduced around that size, due to the hardening of Co bonds, further favoring the GMR. Our analysis gives direct structural parameters and emphasizes their role in the transport and magnetic properties of the Co-Cu system.

I. INTRODUCTION

Artificial composite materials formed by the combination of magnetic and nonmagnetic elements exhibit very exciting physical properties. Magnetic anisotropy, magnetic moment enhancement, superparamagnetic (SPM) or ferromagnetic behavior, depending on size and temperature, and magnetic exchange coupling are just a few important physical aspects that insert these materials at the frontier of research. Among the most remarkable questions concerning these materials are the conditions leading to the phenomenon of giant magnetoresistance (GMR), discovered in magnetic multilayers more than a decade ago.[1] The GMR phenomenon refers to a very large modification in the electrical resistivity when a magnetic field is applied. Subsequently, GMR was also observed in granular magnetic composites, prepared by sputtering,[2–4] and melt-spinning[5–7] techniques, with magnitudes comparable to those found in multilayered systems. The effect is understood in terms of the spin-dependent scattering of the electrons at interfaces, impurities, and, to a lesser extent, within the magnetic elements.[8–11]

Cobalt and copper form a granular magnetic system with nanoscale clusters of Co atoms embedded in the nonmagnetic Cu matrix. Such a system displays one of the largest values for the GMR found in granular systems. This property is a consequence of the macroscopic magnetization, and thence it is related to the cluster-size distribution and to intergranular magnetic interactions.[12–14] Besides the magnetic properties, questions related to the shape and size of the particles, to the structural parameters, and to the mechanism of crystal nucleation and growth[15–18] are crucial to fine-tuning

the properties of the material. Naturally, the burning question is how these structural and morphological properties relate to the amplitude of the GMR effect. Spin-dependent electron scattering at interfaces seems to be the most relevant parameter in the GMR description.[8–11] The amount of interface in granular systems depends on the shape and size of the particles and on their distribution. An atom probe-field ion microscope (AP-FIM) was recently used to study the morphology of particles in the range of 1–10 nm and a reasonable agreement with the theoretical model of GMR behavior related to the diameter of the particle was found.[19,20] Nevertheless, the size of the particles is not the only important parameter: the degree of organization at the interfaces, roughness, magnetic moment changes, magnetic interactions, and detailed microstructure are also relevant parameters to fully understand the involved physics of GMR.[21–23]

There has been a large effort in investigating the morphology and structure of the Co particles in Cu using techniques such as transmission electron microscopy (TEM),[16,18] x-ray diffraction,[6] and small-angle x-ray scattering.[15] However, it is inherently difficult to characterize the Co-Cu system employing scattering and diffraction techniques because of the similarity of their atomic scattering factors and the small lattice mismatch between the Co and Cu compact structures. Many striking features, like the detailed microstructure, intermixing, or roughness at the interface, and extension of magnetic interactions, remain to be tackled. X-ray absorption fine structure (XAFS) spectroscopy is a local and selective tool, capable of probing the local environment of a selected atomic element.[24,25] The similarity between Co and Cu atoms can be turned into an advantage when using the XAFS spec-

troscopy. The low electronic contrast, similar metallic radius, and local arrangement allow one to treat both atoms as identical scatters and use the same backscattering amplitudes and phase shift functions in the analysis.[26] XAFS has already been applied to study the evolution of Co particles in granular alloys.[27–29] The conclusions were that, in the range of Co content up to 15 at. %, Co atoms segregate into small particles, keeping the fcc packing arrangement, with a systematic contraction in the average nearest-neighbor distance around Co as the thermal annealing is increased. However, this trend has not been directly correlated to the transport and magnetic properties of the system.

In this work, the structural and magnetic properties of Co particles embedded in a Cu matrix were studied using XAFS spectroscopy and macroscopic magnetization and then correlated to transport measurements. There is a systematic contraction of the average distance around Co, with increasing Co content and annealing, which is correlated to the growth of the particles and the evolution of the SPM behavior. The average nearest-neighbor distance and disorder obtained from XAFS are linked to the average Co particle size through a simple model and lead to particle sizes ranging from 1 nm to more than 8 nm. Analysis based on the magnetization measurements leads to particle sizes up to 3 nm,[29] because such analysis gives only the average size of the SPM particles. The GMR behavior, measured at room temperature and at 4 K for 10 at. % Co samples, has been directly correlated to those sizes and leads to the conclusion that the GMR effect reaches a maximum for average particles of about 4.4 nm. This value seems to optimize the GMR because the particles are sufficiently large to change orientation under an applied magnetic field and have still a large amount of surface to effectively scatter the conducting electrons. Nevertheless, an additional parameter, the thermal and structural disorder, which can be related to the matrix lattice dynamics, particle-size distribution, and interface roughness, has to be considered to understand the magnetic and magnetotransport properties.

II. SAMPLES

Samples containing 3, 10, 12, and 25 at. % Co embedded in a Cu matrix (named here as Co_3Cu_{97}, $Co_{10}Cu_{90}$, $Co_{12}Cu_{88}$, and $Co_{25}Cu_{75}$, respectively) were produced by rapid quenching using the melt-spinning technique. They have the shape of thin metallic ribbons, 10 mm long by 5 mm wide, with a thickness of about 50 μm. At room temperature, the Co atoms form a metastable phase diluted within a well-crystallized Cu matrix. Co mobility within the matrix can be activated by thermal annealing, leading to the diffusion and segregation of cobalt into small particles. Thermally treated samples display typically GMR ratios up to 30% at low temperatures.[5–7] Instead of heating up the samples using the conventional resistive furnace, the dc Joule heating treatment was applied.[30] This technique gives the amount of energy needed for the mobility in a rather short period of time compared to the conventional technique.[31,32] The Co-Cu samples studied here were annealed by applying, during 1 min, a constant current passing
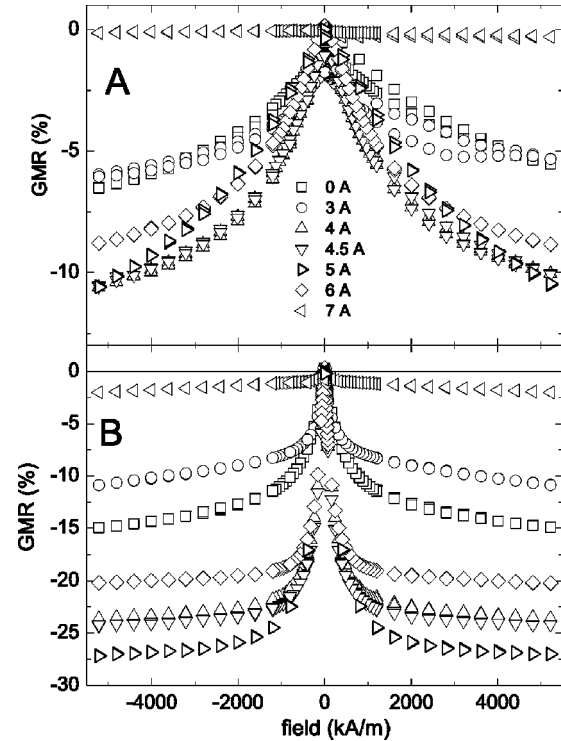

FIG. 1. Magnetoresistance of the $Co_{10}Cu_{90}$ sample at 300 K (A) and 4 K (B), for different currents used in the Joule heating.

through them. The samples are labeled by the current used in the annealing (the as-quenched sample will be referenced as 0 A). X-ray diffraction characterization performed on a few selected $Co_{10}Cu_{90}$ and $Co_{25}Cu_{75}$ samples showed the characteristic fcc pattern imposed by the Cu matrix. No hcp phase was observed for the $Co_{10}Cu_{90}$ series, which has been confirmed by the fingerprint of the near-edge spectra measured on the same samples[29] and also by the XAFS data presented in Sec. IV.

III. TRANSPORT AND MAGNETIC PROPERTIES

Magnetic and transport characterization has been performed using a Quantum Design MPMS XL7 superconducting quantum interference device (SQUID) magnetometer. The magnetic field behavior of the electrical resistance has been characterized by using the four-point scheme to measure the resistance and applying the magnetic field in the plane of the ribbon, perpendicular to the bias current. These magnetoresistance measurements were performed on most of the Joule-treated $Co_{10}Cu_{90}$ samples, at 300 K and 4 K (Fig. 1). These samples present a rather large GMR ratio, defined here as $\Delta R/R[\%] = 100 \times [R(H=5000 \text{ kA/m}) - R(H=0)]/R(H=0)$, with a maximum module of about 27% at 4 K and 11% at 300 K, reached for the 5-A sample (Fig. 2). Within the 4–5-A Joule-treated samples, the GMR is still large and comparable to the its maximum value.

The GMR dependence on the magnetic field is sensitive to the amount of blocked and unblocked particles, with a strong dependence on temperature.[6,12] Blocked particles are easily aligned with a rather small magnetic field and contrib-
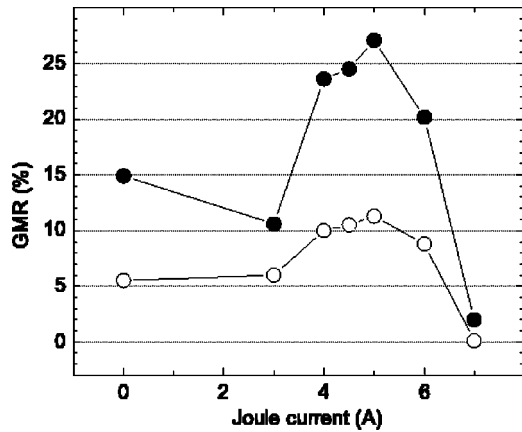
FIG. 2. Maximum value of the GMR at 300 K ($\bigcirc$) and 4 K ($\bullet$) obtained at 5000 kA/m (≈ 6.5 T) as a function of the current used in the Joule annealing, for the $Co_{10}Cu_{90}$ samples.

ute to the low-field region to the GMR effect. Unblocked SPM particles tend to be aligned by the magnetic field against the thermal disorder. As the temperature decreases, more Co particles become blocked and the width of the GMR curve becomes narrower. It can be noticed that the resistance values do not saturate, even at 4 K [Fig. 1(B)], at the maximum applied magnetic field, which accounts for a rather large amount of very small SPM particles.

The magnetization measurements at 300 K (Fig. 3) clearly show that the system behaves as a typical superparamagnet with a large fraction of unblocked Co particles. The magnetization approaches more quickly the saturation for samples annealed with increasing currents, which is the indication of the clustering of Co atoms within the Cu matrix. One can notice that for all samples a hysteresis has been systematically observed, superimposed onto the SPM behavior (inset of Fig. 3). This hysteretic contribution can arise from single-domain particles that are blocked at that temperature. Magnetic dipolar interactions can also play an important role in such a behavior.[13]

The magnetization data have been fitted using a model function that assumes the existence of two magnetic
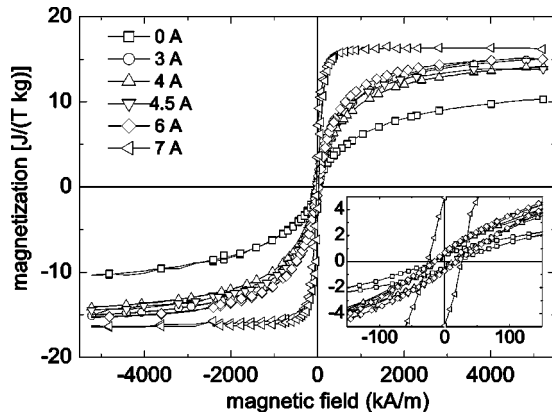

FIG. 3. Magnetization results for the $Co_{10}Cu_{90}$ samples, annealed with different currents, at 300 K. The inset is a close-up of the region near the origin, in order to show the hysteretic behavior.

phases:[14,33] a SPM phase formed by a distribution of small, unblocked ferromagnetic particles and a ferromagnetic (FM) phase formed by large blocked particles. The results, published in detail elsewhere,[29] show that the average magnetic moment of the SPM particles increases as the annealing current increases. Assuming that the SPM particles are spherical and taking the saturation magnetization for bulk fcc Co, their average diameter D_{SPM} has been estimated. As expected from the magnetic behavior, a growing particle size has been obtained as the annealing current increases. However, the average diameter obtained turn out to be limited to a maximum value of 3 nm.[29] This is because, even at room temperature, a fraction of particles are blocked and do not contribute to the SPM behavior.

IV. X-RAY ABSORPTION FINE STRUCTURE

A. Experiment

XAFS measurements were carried out around the Co K edge for series of Co_3Cu_{97}, $Co_{10}Cu_{90}$, $Co_{12}Cu_{88}$, and $Co_{25}Cu_{75}$ samples. Each series was submitted to different thermal annealing. The measurements were performed at the XAS beamline[34] at the Brazilian Synchrotron Light Laboratory (LNLS) running at 1.37 GeV and with an average stored current of 150 mA. The photon energy was selected using a Si(111) channel-cut crystal monochromator, which provided an instrumental energy resolution of about 1.5 eV at 7709 eV. All samples were measured at room temperature (RT) in transmission mode, with ionization chambers as incident and transmitted beam detectors. The beam size, illuminating the sample at 14 m from the source, was about 5 mm horizontal by 0.5 mm vertical. Co and Cu metal foils were measured as reference compounds. In order to evaluate the thermal and static disorder contributions, the references and one $Co_{10}Cu_{90}$ sample were measured at 8 K, using a closed-cycle cryorefrigerator.

B. XAFS signal

The oscillatory fine structure of an x-ray absorption spectrum, the XAFS signal $\chi(k)$, is given by $[\mu(k) - \mu_0(k)]/\mu_0(k)$, where k is the photoelectron wave number modulus $[k = \sqrt{(2m/\hbar^2)(E - E_k)}$; E_K is the energy of the K edge], $\mu(k)$ the absorption coefficient, and $\mu_0(k)$ the so-called atomic absorption coefficient. The XAFS signal depends on several parameters and can be obtained in its simplest way as a summation over all interference patterns scattered off by all neighboring atoms.[24,25] These neighboring atoms are considered to form shells around the absorbing central atom:

$$\chi(k) = \sum_j \left(\frac{S_0^2 N_j}{k R_j^2} \right) F_j(k) \exp(-2k^2 \sigma_j^2)$$

$$\times \exp\left(\frac{-2R_j}{\lambda(k)} \right) \sin[2k R_j + \phi_j(k)]. \quad (1)$$

Here R_j is the average distance between the absorbing central atom and the jth shell, with a Gaussian rms deviation
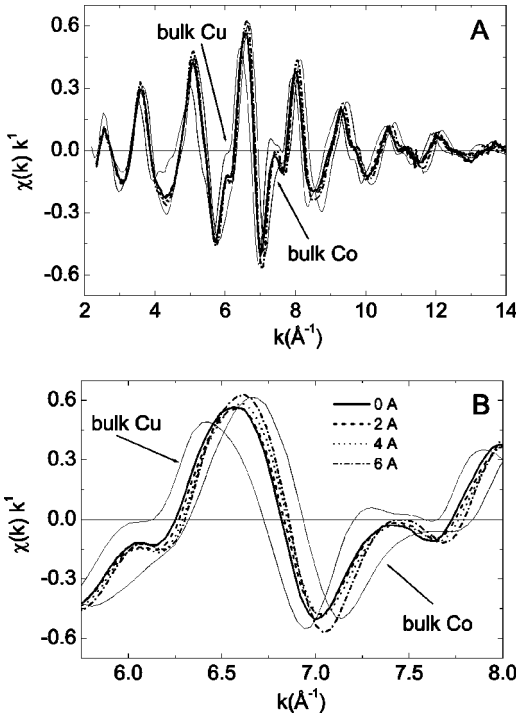
FIG. 4. XAFS signal extracted from the raw absorption spectra of some representative $Co_{10}Cu_{90}$ samples. The upper panel displays the signal in the whole range used in the data analysis, while the bottom panel shows an enlarged region, where one can compare the signal of the samples with those of bulk Cu and Co.
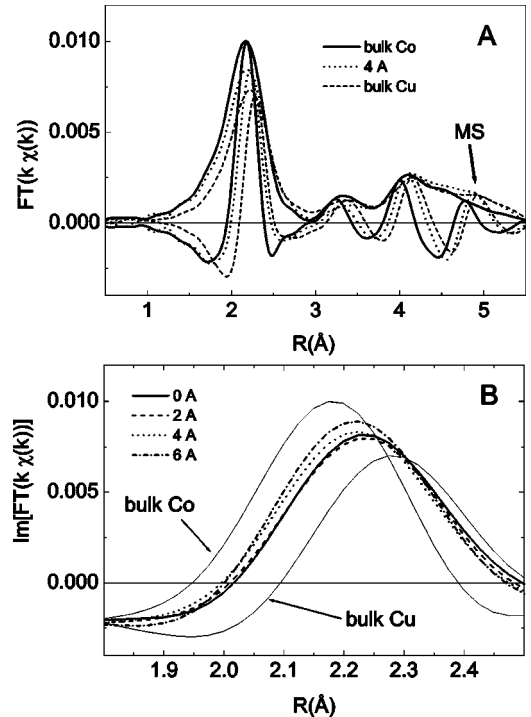

FIG. 5. Fourier transform of the XAFS signal displayed in Fig. 4. One can observe in the upper panel the imaginary part and modulus of both Co and Cu bulk metals and the $Co_{10}Cu_{90}$ sample, Joule treated with 4 A. One should note also the indication of multiple scattering (MS) in the fourth shell, which indicates the fcc structure adopted by the Co atoms within the particles. In (B) only the imaginary part of the coordination peak is enlarged to emphasize the variation of the distance observed in the samples, between those of the bulk Cu and Co.

from the average distance expressed by σ_j, which accounts for the thermal and static disorder; N_j is the number of atoms in the jth shell, with backscattering amplitude $F_j(k)$; S_0^2 is the amplitude reduction factor due to photoelectron correlation; $\lambda(k)$ is the mean free path of the photoelectron; and $\phi_j(k)$ is the total phase shift. The first shell of atoms, named the coordination shell, is well described by the theory involving only single scattering of the photoelectron. For farther shells, multiple scattering can give important contributions, especially on these well-ordered and compact structures.[24]

C. XAFS analysis

The data analysis was performed using the WINXAS code.[35] A straight line, fitted in the pre-edge region, was subtracted from the raw spectra, which were then normalized to the edge jump in a knot of the initial oscillations (about 20 eV above the edge). The edge energy E_K was determined choosing the first inflection point in the edge region of the spectra and energy-dependent spectra $\mu(E)$ were turned into the photoelectron wave number modulus dependence $\mu(k)$. Then, XAFS signals were extracted, fitting a five-segment cubic spline above the edge. The net XAFS oscillations at RT for some selected $Co_{10}Cu_{90}$ samples are shown in Fig. 4(A). The two reference samples, Co and Cu metal standards, are shown for comparison. The Co K-edge fine structure of Co-Cu samples resembles that of the bulk Cu, with a slightly different frequency (or distance) [Fig. 4(B)]. This similarity is evidence that the structure around Co atoms assumes the fcc packing, rather than the hcp one, of the bulk Co. Nevertheless, one can remark that the XAFS amplitudes are closer to that of bulk Co, pointing out that, on average, there are more Co than Cu neighbors surrounding Co atoms in these samples.

The XAFS signal, from 3.3 to 14 $Å^{-1}$, weighted by the photoelectron wave number k, was analyzed using the Fourier transform (FT) technique, applying a Hanning apodization window, with parameter 20. The modulus and imaginary parts of the FT are displayed in Fig. 5(A). For the sake of clarity, in Fig. 5(A) only one intermediate sample was selected to compare to the standards. Figure 5(B) shows the imaginary part, around the coordination shell, for selected $Co_{10}Cu_{90}$ samples. In range of the coordination-shell contribution, the samples are between both standards, with intermediate average distance and slightly reduced amplitude compared to the bulk Co. The small reduction in amplitude of FT's for the coordination shell, which is accompanied by an increase in the width of the peak, is related to the small increase of disorder. The second important remark concerns the more distant shells. It is known that, due to the focusing effect,[24,25] the fcc structure has a strong multiple-scattering (MS) contribution in the region of the fourth shell, enhancing the FT amplitude in that region compared to the hcp structure. This MS effect is clearly observed in the Co-Cu

samples, showing that the packing is indeed fcc. The existence of this MS effect indicates, in addition, that the structural disorder is very small compared to the bulk crystalline samples.

In order to obtain the quantitative structural parameters for the Co-Cu samples, the peak in the FT corresponding to the coordination-shell contribution (from 1 to 3 Å) was selected and backtransformed into k space. A standard nonlinear least-squares fit was applied to simulate to the Fourier-filtered data.[35] The parameters R and N stand for the average coordination distance and average coordination number, respectively. $\Delta\sigma^2$ represents the disorder, or Debye-Waller factor, relative to the reference sample used in the fit. The phase shift and amplitude extracted from the Fourier-filtered experimental spectrum of bulk Co at RT was used as reference. The parameters R and $\Delta\sigma^2$, as well as the origin of the energy ΔE_K, were allowed to vary during the fit, while N was kept equal to 12. The reported error bars were estimated by the standard parabola method with a confidence interval imposed to be larger than 68%.

D. XAFS results

The results of the best-fit analysis for the unknown parameters R, $\Delta\sigma^2$, and ΔE_K (average distance, relative Debye-Waller factor, and edge-energy correction), with $N = 12$, are shown in Table I for the Co_3Cu_{97}, $Co_{10}Cu_{90}$, $Co_{12}Cu_{88}$, and $Co_{25}Cu_{75}$ samples. In all series studied, we observed significant differences in the Co neighborhood, related to R and $\Delta\sigma^2$, which are summarized in Fig. 6.

1. Average nearest-neighbor distance

The Co average nearest-neighbor distance (R) varies from the Cu-Cu bond distance ($R_{Cu} = 2.556$ Å) to close that of the fcc Co-Co bond ($R_{Co} = 2.504$ Å), according to the Co content and annealing conditions [see Fig. 6(A)]. For the Co_3Cu_{97} samples, the average distance is kept essentially equal to that of Cu-Cu bond. Only the last two samples, Joule treated at 5.5 A and 6.0 A, show a reduction in the average distance, indicating the formation of Co-Co bonds. For the $Co_{10}Cu_{90}$ samples, the average distance is smaller than that of Cu even for the as-quenched sample and shows a decrease as the Joule current increases. Around 5–7 A a plateau is observed and above 7 A the average distance is much closer to that of bulk fcc Co. For the $Co_{12}Cu_{88}$ samples, the behavior is very similar to the $Co_{10}Cu_{90}$ samples with a bit smaller average distance. For the $Co_{25}Cu_{75}$ samples, the average distance does not display significant variations with increasing annealing. It is close to the bulk Co value, meaning that most Co atoms are bonded to Co. In fact, one can notice that the average distances are between those from the fcc (2.504 Å) and hcp (2.494 Å) phases, and it can be inferred that, for such a concentration, the hcp phase starts to develop. These results can be understood in the following way. For as-quenched samples there is a trend of R towards the bulk Co interatomic distance as the Co content increases. For Co_3Cu_{97} samples, the Co atoms are dispersed in the Cu matrix, simply substituting Cu atoms. For higher Co contents, there is a tendency for Co atoms to

TABLE I. XAFS results. R is the first-neighbor average distance, $\Delta\sigma^2$ is the relative Debye-Waller factor, and ΔE_K is the absorption-edge energy correction. The coordination number was fixed at the Co bulk value (12). The error bars in distance, Debye-Waller factor, and ΔE_K fluctuate for each sample, but are always smaller than ± 0.003 Å, $\pm 3 \times 10^{-4}$ Å^2, and ± 0.2 eV, respectively.

Joule current (A)	R (Å)	$\Delta\sigma^2$ ($\times 10^{-4}$ Å^2)	ΔE_0 (eV)
	Co_3Cu_{97}		
0	2.557	23	2.1
2	2.552	23	1.6
4	2.556	20	2.0
4.5	2.559	19	2.2
5	2.555	24	2.4
5.5	2.543	22	1.6
6	2.538	21	1.4
	$Co_{10}Cu_{90}$		
0	2.538	15	1.0
2	2.530	17	0.6
3	2.526	16	0.4
4	2.521	14	0.3
5	2.518	10	−0.1
6	2.519	7	0.0
7	2.518	4	0.1
9	2.511	2	−0.1
	$Co_{12}Cu_{88}$		
0	2.524	16	0.5
3.5	2.512	12	0.4
4	2.516	13	0.5
4.5	2.513	12	0.7
5	2.515	13	0.5
6	2.511	9	0.2
	$Co_{25}Cu_{75}$		
0	2.497	6	0.1
5	2.500	9	0.0
6	2.499	3	0.2
7	2.498	8	0.0
8	2.502	3	0.6
9	2.498	2	0.4

segregate into particles. When the concentration reaches 25 at. % Co ($Co_{25}Cu_{75}$ samples), the particles are big enough so that the number of Co-Co bonds dominates completely. For the Joule-treated samples, the thermal energy gives mobility to the Co atoms and allows their coalescence, leading to an increase in the particle size and a reduction of R towards the bulk Co average distance. This behavior is well illustrated by the $Co_{10}Cu_{90}$ series. The behavior of the Co_3Cu_{97} samples indicates that much more thermal energy is necessary to form Co particles, with the appearance of a significant number of Co-Co bonds only for annealing current higher than 5 A. For the $Co_{25}Cu_{75}$ series, the particle sizes are big enough so that XAFS does not sense the increasing in the particle
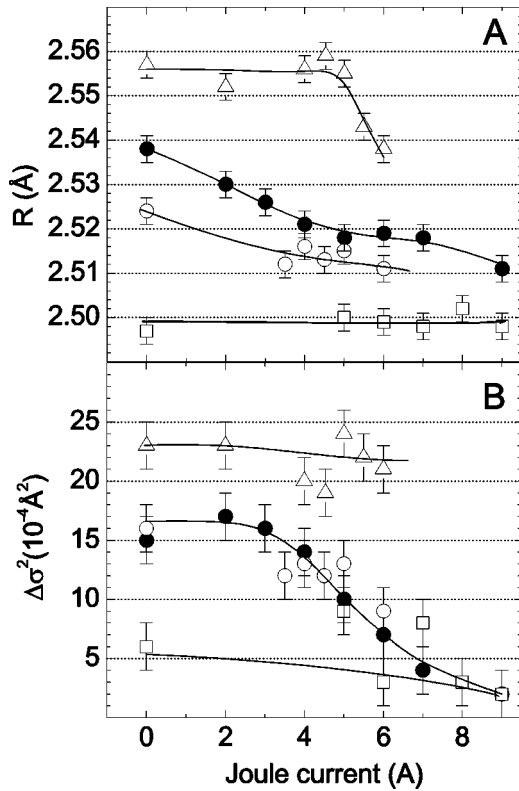
FIG. 6. Resulting neighbor distances (R) and relative Debye-Waller factors ($\Delta\sigma^2$) from the fitting of the XAFS equation [Eq. (1)] to the XAFS signal of the coordination shell, obtained from the first peak of the Fourier transform backtransformed into k space. The different symbols hold for the Co_3Cu_{97} ($\triangle$), $Co_{10}Cu_{90}$ ($\bullet$), $Co_{12}Cu_{88}$ ($\circ$), and $Co_{25}Cu_{75}$ ($\square$) samples. The lines are just guides for the eyes.

size due to the thermal annealing. These results are in agreement with Monte Carlo simulations.[17]

2. Relative Debye-Waller factor

Another important issue is the behavior of the relative Debye-Waller factor $\Delta\sigma^2$. As can be seen in Fig. 6(B), for the $Co_{25}Cu_{75}$ samples $\Delta\sigma^2$ is very small, close to zero, which means that the disorder is almost that of bulk Co. For the lowest-concentration Co_3Cu_{97} sample, $\Delta\sigma^2$ has the highest values. Even upon annealing, they are kept roughly constant. In this case, Co atoms are mainly replacing Cu atoms and only small clusters (dimmers, trimmers, etc.) may develop. Essentially all Co atoms are bonded directly to the Cu matrix. A more interesting situation takes place in the case of intermediate $Co_{10}Cu_{90}$ and $Co_{12}Cu_{88}$ concentrations. $\Delta\sigma^2$ is halfway between the Co_3Cu_{97} and $Co_{25}Cu_{75}$ series. For the as-quenched and weakly annealed $Co_{10}Cu_{90}$ samples $\Delta\sigma^2$ is almost constant, but it starts to decrease around the 3–4-A Joule-treated samples. In the range of thermal annealing from 4 to 7 A, while R gets to an almost constant value, $\Delta\sigma^2$ decreases monotonically down to close to zero.

In XAFS the Debye-Waller factor comes from structural and thermal disorders ($\sigma^2 = \sigma_{ST}^2 + \sigma_{TH}^2$), which enter equivalently in the theory and cannot be separated in the

analysis.[24,25] The thermal disorder depends on the dynamical properties of the lattice and can vary significantly from one matrix to another.[36,37] The fact that σ^2 found for the $Co_{25}Cu_{75}$ samples is close to the bulk Co is not surprising. The contribution to σ^2 is mainly coming from well-ordered large nanoparticles, whose thermal behavior is nearly the same as the bulk Co and whose structural component is negligible. For the Co_3Cu_{97}, $Co_{10}Cu_{90}$ and $Co_{12}Cu_{88}$ samples, the additional $\Delta\sigma^2$ found can be assigned to two origins: first, it can arise from a static disorder or bond-length dispersion at interfaces; second, it can be of thermal origin and depends on the nature of the neighboring atoms bound to Co. In both cases, $\Delta\sigma^2$ depends on the surface-to-volume ratio.

The thermal behavior around Co atoms evolves from a situation where Co atoms are diluted within the Cu matrix to another one where they are within large Co nanoparticles. The thermal Debye-Waller factor for Cu is greater than for Co,[37] and the experimental $\Delta\sigma^2$ cannot be associated entirely to an interfacial disorder. To get more insight into this point, the Co and Cu metal standards and the 6-A Joule-treated $Co_{10}Cu_{90}$ sample were also measured at 8 K. The thermal contribution to the disorder at RT compared to 8 K [$\Delta\sigma_{TH}^2 = \sigma^2(RT) - \sigma^2(8\,K)$] for bulk Co and Cu was found to be 0.0034 and 0.0047 Å^2, respectively, which confirms that Co-Co bonds are stiffer than Cu-Cu bonds.[37] In the case of the 6-A $Co_{10}Cu_{90}$ sample, $\Delta\sigma_{TH}^2$ was found to be 0.0036 Å^2, very close to the Co bulk value, showing that sufficiently large Co nanoparticle thermally behaves like bulk Co. Nevertheless, when Co is diluted within the Cu matrix or forming small nanoparticles, it behaves like Cu in bulk Cu, with an increased thermal Debye-Waller factor compared to the Co matrix. This is the case of the Co_3Cu_{97} samples, whose increase in disorder, compared to Co in bulk Co at RT, is about 0.0023 Å^2 [Fig. 6(B)]. Thence, we can argue that the measured values for $\Delta\sigma^2$ are essentially of thermal origin and are associated to a softening of the modes due to the amount of Co atoms bound directly to the Cu matrix, with some smaller structural contribution.

E. Model for Co particles within a Cu matrix

We present here a simple quantitative model to associate the measured average distance and relative Debye-Waller factor to the average particle size. Contrary to other models for estimating particle size using the reduction in the coordination number,[38,39] our model is based upon a contraction on distances. Owing to the similarity among Co and Cu structures, the coordination number must be the same, independent of the structural changes of the system. The average nearest-neighbor distance and disorder depend on the relative number of Co-Co and Co-Cu bonds. In order to count this relative number, we propose a model for closed-shell particles, separating the Co atoms forming particles into two categories: (i) those within the surface (or interface) of the particles and (ii) those within the core of the particles. The atoms in the first category have, as nearest neighbors, Cu (outside the particle) and Co (inside the particle) atoms, whereas the second category of Co atoms have just Co nearest neighbors. The average distance and relative disorder

measured by XAFS around Co atoms depend on the proportion of the first to the second categories. As the Co particle size increases, the surface/volume ratio decreases and the second category of Co atoms weights the average towards the bulk Co interatomic distance and to a smaller overall structural disorder. Experimentally, we have already pointed out that both average distance and disorder tend to decrease with the increase of Co content and annealing.

The basic assumption, which turns the model very simple, is that the small mismatch (2% or $\Delta R = R_{Cu} - R_{Co} = 0.052$ Å) of Cu ($R_{Cu} = 2.556$ Å) and Co ($R_{Co} = 2.504$ Å) bonds is totally absorbed by the atoms within the particle surface. This assumption has support from studies of Co/Cu multilayers, where the Co-Co bonding perpendicular to the surface relaxes rapidly to the bulk bonding,[26,40] and from x-ray diffraction data on a Co-Cu system, where the Co-rich phase has the lattice parameter close to the fcc Co phase.[28] This means that inner atoms of sufficiently large particles retain the bulk Co distance and only the surface Co atoms relax to accommodate to the matrix. Consequently, one should differentiate among three nearest-neighbor environments for Co atoms forming particles: (i) Co atoms forming the core of the particle have the bulk Co average distance (R_{Co}) and no bond-length dispersion; (ii) surface Co atoms have average distance equal the bulk Cu (R_{Cu}), despite their distorted neighborhood, because the mismatch is accommodated in such a way that the distance to Cu outside is longer ($R_{Cu} + \Delta R/2$) than the distance to Co inside the particle ($R_{Co} + \Delta R/2$); (iii) intermediate Co atoms, those forming the shell of atoms just below the surface, have an intermediate distance $R_I = R_{Co} + \Delta R/4$—that is, the average between R_{Co}, to core Co atoms, and $R_{Co} + \Delta R/2$, to surface Co atoms. The last two environments for Co atoms have bond-length dispersions that are taken into account by a static Debye-Waller factor. In such a way, small particles—i.e., formed by three to four shells—are enabled to have a continuous relaxation from the core to the surface. For large particles, this relaxation is still taken into account in the outmost shells but becomes less relevant.

Following such model, the expected average distance is given by

$$R_M = \frac{N_S R_{Cu} + N_I R_I + N_C R_{Co}}{N_S + N_I + N_C}, \quad (2)$$

TABLE II. Closed-shell fcc clusters. N_T and N_S are the total number of atoms in the whole particle and on the surface, respectively. N_I (not listed in this table) used in Eqs. (2) and (3) is the number of atoms in the shell just below the surface, in such a way that for the nth shell, N_I is the value of N_S for the $(n-1)$th shell. D_{CSP} is the diameter of the cluster taking into account the fcc Co interatomic distance (2.504 Å).

Shell	N_T	N_S	$\dfrac{N_S}{N_T}$	D_{CSP} (nm)
0	1	1	1	0.25
1	13	12	0.923	0.75
2	55	42	0.764	1.1
3	147	92	0.626	1.5
4	309	149	0.482	1.9
5	561	246	0.439	2.3
6	923	349	0.378	2.7
7	1415	498	0.352	3.2
8	2057	629	0.306	3.6
9	2869	825	0.288	4.0
10	3871	989	0.256	4.4
11	5069	1230	0.243	4.8
12	6521	1477	0.227	5.2
13	8134	1726	0.212	5.6
14	10 150	2026	0.200	6.0
15	12 330	2323	0.188	6.4
16	14 990	2674	0.178	6.8
17	17 815	3018	0.169	7.2
18	21 000	3386	0.161	7.6
19	24 450	3762	0.154	8.0

where N_S, N_I, and N_C are the surface, intermediate, and core number of Co atoms forming the particle. Based on the sequence of closed-shell particles (CSP's) for the fcc Co packing (Table II), which can be approximated to spherical particles of diameter D_{CSP}, and Eq. (2), we can calculate the expected average distance (R_M) for a given particle size [Fig. 7(A)]. The model can also be applied to calculate the bond-length dispersion or static disorder. The squared rms deviation from R_M, which gives the bond-length dispersion, is calculated taking the summation

$$\Delta \sigma_{ST}^2 = \frac{N_S (R_{Cu} - R_M)^2 + N_I (R_I - R_M)^2 + N_C (R_{Co} - R_M)^2}{N_S + N_I + N_c}. \quad (3)$$

The model predicts that for Co atoms isolated within the Cu matrix, or small Co particles, the average distance is close to the bulk Cu bond and the static disorder is nearly zero. As particles grow, the distance tends to the bulk Co bond, while the static disorder increases, reaches a maximum and then, for large particles, decreases along with the surface/volume ratio [Fig. 7(B)]. It is assumed here that the static disorder of the fcc matrix is negligible, so that σ_{ST}^2 and $\Delta \sigma_{ST}^2$ are equivalent.

The static disorder alone cannot explain the measured relative Debye-Waller factor. One has to add the contribution coming from the lattice dynamics, associated with the num-
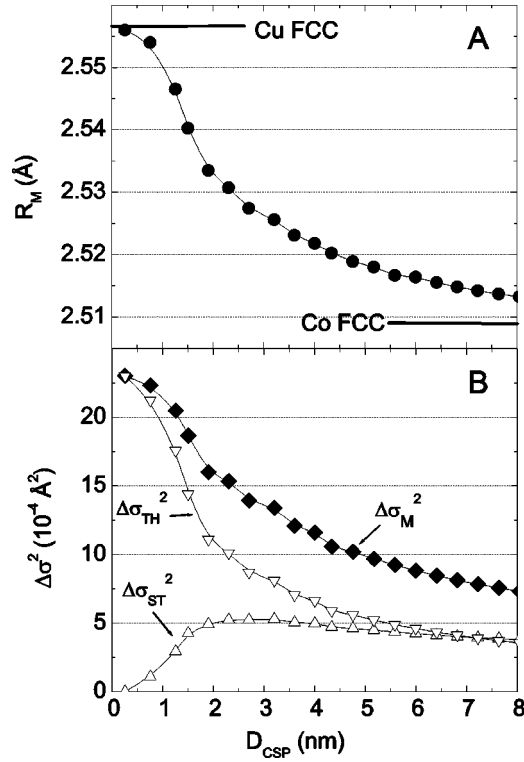
FIG. 7. Results based on the model to estimate the particle size. As the size of the particle increases, the coordination distance (A) and Debye-Waller factor (B) change from values similar to the bulk Cu to values similar to the bulk Co. In panel (B) are displayed the static ($\triangle$) and thermal ($\triangledown$) contributions for the total ($\blacklozenge$) Debye-Waller factor.
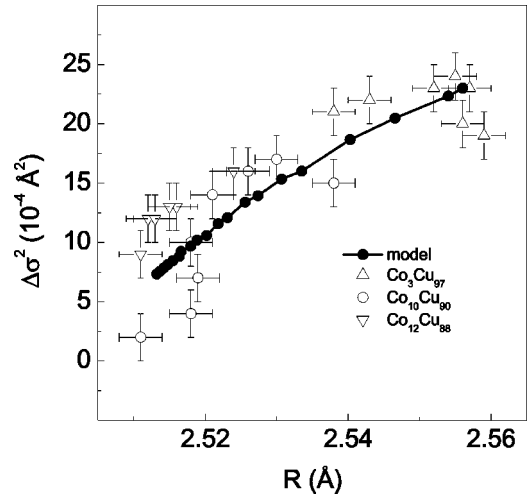

FIG. 8. Correlation between the average coordination distance and the Debye-Waller factor. The solid line connects the points whose coordinates are R_M and $\Delta\sigma_M^2$ for each closed-shell particle. The experimental points come from the XAFS results ($R, \Delta\sigma^2$), from the studied samples.

ber of Co atoms bound to the Cu matrix. When Co particles are very large, the thermal behavior is practically that of bulk Co and $\Delta\sigma_{TH}^2$ is zero. When the Co atoms are individually dispersed within the Cu, the lattice dynamics around Co is controlled by the Cu matrix, and the thermal contribution should be the relative disorder among Cu and Co bulk samples. This value can be taken as the experimental relative Debye-Waller factor found for the Co_3Cu_{97} samples, i.e., $\Delta\sigma^2 \approx 0.0023$ Å^2. This agrees, within the error bar, with the value that can be estimated from Bohmer and Rabe,[37] i.e., $\Delta\sigma^2 \approx 0.003 \pm 0.001$ Å^2. The relative contribution to the thermal disorder is taken as the value $\Delta\sigma^2 \approx 0.0023$ Å^2 weighted by the surface/volume ratio [Fig. 7(B)]. For increasing particle size, the thermal disorder decreases very rapidly, while the static disorder increases, reaching a maximum around 3 nm, and then slowly decreases. Both contributions are comparable for particles larger than 3 nm. However, the thermal fluctuations, owing to the softer bonds to the Cu matrix, completely dominate the total relative disorder ($\Delta\sigma_M^2 = \Delta\sigma_{ST}^2 + \Delta\sigma_{TH}^2$) below that size. This means that the increased rms fluctuation in distance, or disorder, for small nanoparticles has to be mostly associated to the thermal behavior of the matrix, rather than to static disorder at the interface. Indeed, even the maximum mismatch in distance, $\Delta R = 0.052$ Å, is smaller than the rms bond-length fluctuation at RT coming from the absolute thermal Debye-

Waller factor, $\sqrt{\sigma_{TH}^2} = 0.088$ Å, for bulk Cu.[36,37] This fact further justifies our model, where the details of the relaxation at the interface are simplified.

We may note that there is a simple correlation between the R_M and $\Delta\sigma_M^2$ values. The solid line in Fig. 8 is connecting the points whose coordinates are R_M and $\Delta\sigma_M^2$ for each closed-shell particle listed in Table II. One can see that, when the particle size decreases, both R_M and $\Delta\sigma_M^2$ increase. It is also clear that there is a correlation between the experimental average distance (R) and relative disorder ($\Delta\sigma^2$). The experimental points follow the behavior of the calculated curve, demonstrating that the model describes quite well the general trend of the system, further corroborating with the assumptions made in the model, despite their simplicity. On the other hand, one should note that this model can be easily adapted for more sophisticated descriptions of the diffusion of cobalt in copper that can be found in the literature (see Ref. 41, e.g.).

Comparing the average nearest-neighbor distance from XAFS [Fig. 6(A)] with the calculated average distance from the model [Fig. 7(A)], one can estimate, by interpolating data, the average particle diameter (D_{EXA}) for each measured sample. The results are presented in Fig. 9 for the Co_3Cu_{97}, $Co_{10}Cu_{90}$, and $Co_{12}Cu_{88}$ samples as a function of Joule current. One can observe that the average particle diameter is indeed increasing with Co content and annealing current. For the Co_3Cu_{97} samples, Co atoms remain diluted within the matrix up to 5 A and after that segregate, reaching about 2 nm for 5.5 and 6 A. For $Co_{10}Cu_{90}$ samples, the nanoparticles start with a size close to 2 nm for the as-quenched sample up to a value close to 5 nm for 5–7 A and then close to 10 nm for 9 A. For $Co_{12}Cu_{88}$ samples, the nanoparticles start with about 3 nm for the as-quenched sample, grow quickly to about 7 nm for 4–5 A, and then close to 10 nm for 6 A. However, owing to the fact that the average distance quickly converges to a value close to the bulk Co, the error
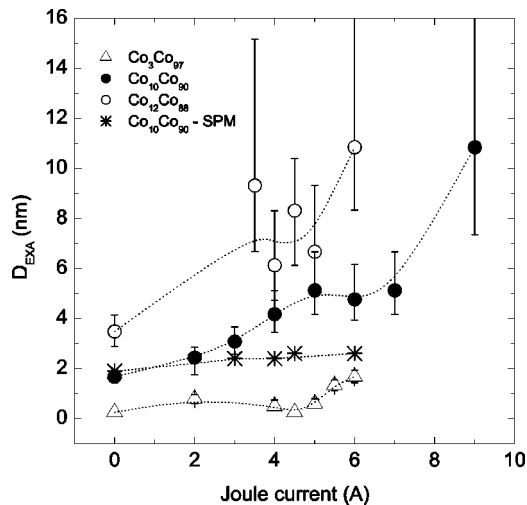
FIG. 9. Average diameter of the Co particle from the comparison of our XAFS results with the values from the model. The lines are just a guide for the eyes. The stars are the results from magnetization data (Ref. 29) for the $Co_{10}Cu_{90}$ samples.

bar becomes excessively large for particles larger than 8–9 nm. An additional increase in the particle diameter reflects itself only as a minor change in the average distance. For that reason, the discussion is limited to particles smaller than 8 nm and the $Co_{25}Cu_{75}$ samples are excluded.

V. DISCUSSION

The average size of the SPM particles for the $Co_{10}Cu_{90}$ samples at RT, as reported by Cezar et al.,[29] is plotted in Fig. 9, along with the results from XAFS. The saturation in their average size, less than 3 nm at RT, is clearly seen and takes place because, even if the average particle size is increasing, only particles below a critical size are contributing to the superparamagnetism. This result is not incompatible with the one obtained by XAFS, which senses all Co atoms, including as well those that are forming large blocked particles as those diluted within the matrix.

In general, the interatomic distances in nanoparticles are not the same as in the bulk. Our assumptions in the model only hold for granular systems where both the matrix and dispersed metal have very similar structural characteristics, as is the case of Cu and Co. The Co assumes a fcc structure as the Cu matrix, with a mismatch in lattice parameter of only 2%. It should be pointed out that our model for estimating nanoparticle sizes from XAFS distances is more reliable for the intermediate sizes because interface details and relaxation are less relevant for particles with more than three to four shells, i.e., larger than 1.0 nm. On the other hand, the model becomes inaccurate for particles larger than 8 nm due to the error bars from the XAFS analysis. Fortunately, interesting samples displaying large GMR fall within this range of sizes.

From the magnetotransport measurements (Fig. 2), one can observe that the maximum GMR effect for the $Co_{10}Cu_{90}$ samples is reached for the annealing current within 4–5 A annealing current. Based on our model and the XAFS results,

these samples have an average Co nanoparticle diameter of $\approx 4.4 \pm 1$ nm (Fig. 9 and Table II), i.e., a surface/volume ratio of about $\approx 0.26 \pm 0.05$. In addition, we observed that the disorder is significantly reduced at that range of annealing currents and this favors the GMR. The reduction in the disorder seems to be mostly of thermal origin and related to a hardening of Co bonds when the particles grow up to a certain level. Both the optimized surface/volume ratio and the reduction of disorder give rise to the pronounced GMR.

For the same annealing conditions, the average particle size increases with the Co content. For instance, within 4–5 A currents, the $Co_{12}Cu_{88}$ samples have an average particle size around 7 nm, while the Co_3Cu_{97} ones have less than 1 nm. As reported in the literature,[7,31,32] the maximum GMR value as a function of the annealing current is practically independent of the Co content in the range of 5–15 at. % Co samples. The same holds for conventional furnace annealing,[6,28,31,32] with the maximum GMR reached within 400–500 °C. This means that, for higher Co content, the maximum GMR is achieved with a higher average nanoparticle size. We can conclude that the average nanoparticle diameter is not the only important parameter to optimize the GMR effect. Indeed, the maximum GMR is achieved owing to a combination of several factors. As the spin-dependent scattering at the interface plays the major role in GMR, the maximum effect in a granular system depends strongly on the size and distribution of particles and on the quality of the interface. Smaller particles display larger surface/volume ratios but, on the other hand, the magnetic moments of very small particles are more difficult to align, due to the thermal energy. Moreover, very small particles may have their magnetic moments reduced due to the matrix.[23] Such factors, combined with the effect of dipolar interactions and the optimal intergranular spacing, give rise to the experimental curve shown in Fig. 2. For a given Co content, in order to maximize GMR, the nanoparticles have to be large enough to react to an applied magnetic field, but should have enough surface, with a minimum amount of disorder—i.e., well-defined magnetic interfaces—to scatter conduction electrons.

VI. CONCLUDING REMARKS

We have studied the structural, magnetic, and transport properties of cobalt nanoparticles embedded in a copper matrix using XAFS spectroscopy, macroscopic magnetization, and transport measurements of samples containing 3, 10, 12, and 25 at. % Co, annealed under different conditions. We observed by XAFS that there is a systematic contraction of the average coordination distance around Co atoms and a decrease in the disorder with the increasing Co content and annealing. These results are consistent with the growing of small fcc Co nanoparticles and correlated to the evolution in the superparamagnetic behavior. We presented a simple model to correlate the diameter of the Co nanoparticles to the average coordination distance and to its mean-square fluctuation. Our analysis, based on the structural model, leads to cluster sizes ranging from 1 nm to more than 8 nm. We found that the maximum GMR, for samples containing 10 at. % Co, occurs for nanoparticles with diameter of about 4.4 nm. This

corresponds to about 26% of the Co atoms at the particle-matrix interface. This size optimizes the GMR because the particles are sufficiently large to change orientation under an applied magnetic field and have a large amount of surface to magnetically scatter the conducting electrons responsible for the transport properties. Nevertheless, the average nanoparticle diameter is not the only important parameter to optimize the GMR effect. For instance, the maximum GMR is achieved with a higher average nanoparticle size for samples with higher Co content. In addition, we observed that the mean-square fluctuation, or the disorder, is significantly reduced around that size (4.4 nm), further favoring the GMR.

Moreover, our analysis indicates that the disorder is not mainly connected to the static bond-length variation at interfaces, but rather to the thermal fluctuation.

---

*Electronic address: helio@lnls.br

[1] M.N. Baibich, J.M. Broto, A. Fert, F.N.V. Dau, F. Petroff, P. Eitenne, G. Creuzet, A. Friederich, and J. Chazelas, Phys. Rev. Lett. **61**, 2472 (1988).

[2] A.E. Berkowitz, J.R. Mitchell, M.J. Carey, A.P. Young, S. Zhang, F.E. Spada, F.T. Parker, A. Hutten, and G. Thomas, Phys. Rev. Lett. **68**, 3745 (1992).

[3] J.Q. Xiao, J.S. Jiang, and C.L. Chien, Phys. Rev. Lett. **68**, 3749 (1992).

[4] C.L. Chien, J.Q. Xiao, and J.S. Jiang, J. Appl. Phys. **73**, 5309 (1993).

[5] J. Wecker, R. von Helmolt, L. Schultz, and K. Samwer, Appl. Phys. Lett. **62**, 1985 (1993).

[6] R.H. Yu, X.X. Zhang, J. Tejada, M. Knobel, P. Tiberto, and P. Allia, J. Appl. Phys. **78**, 392 (1995).

[7] P. Allia, M. Baricco, M. Knobel, P. Tiberto, and F. Vinai, J. Magn. Magn. Mater. **140**, 617 (1995).

[8] S.F. Zhang and P.M. Levy, J. Appl. Phys. **69**, 4786 (1991).

[9] S.F. Zhang and P.M. Levy, J. Appl. Phys. **73**, 5315 (1993).

[10] M. Rubinstein, Phys. Rev. B **50**, 3830 (1994).

[11] R.Y. Gu, D.Y. Xing, and J.M. Dong, Solid State Commun. **98**, 391 (1996).

[12] B.J. Hickey, M.A. Howson, S.O. Musa, and N. Wiser, Phys. Rev. B **51**, 667 (1995).

[13] P. Allia, M. Coisson, M. Knobel, P. Tiberto, and F. Vinai, Phys. Rev. B **60**, 12 207 (1999).

[14] A.D.C. Viegas, J. Geshev, L.S. Dorneles, J.E. Schmidt, and M. Knobel, J. Appl. Phys. **82**, 3047 (1997).

[15] T.A. Rabedeau, M.F. Toney, R.F. Marks, S.S.P. Parkin, R.F.C. Farrow, and G.R. Harp, Phys. Rev. B **48**, 16 810 (1993).

[16] A. Hutten and G. Thomas, Ultramicroscopy **52**, 581 (1993).

[17] F.C.S. da Silva, E.F. Ferrari, and M. Knobel, J. Appl. Phys. **86**, 7170 (1999).

[18] R. Busch, F. Gartner, C. Borchers, P. Haasen, and R. Bormann, Acta Metall. Mater. **43**, 3467 (1995).

[19] W.D. Wang, F.W. Zhu, J. Weng, J.M. Xiao, and W.Y. Lai, Appl. Phys. Lett. **72**, 1118 (1998).

[20] W.D. Wang, F.W. Zhu, W.Y. Lai, J.Q. Wang, G.Y. Yang, J. Zhu, and Z. Zhang, J. Phys. D **32**, 1990 (1999).

[21] R. Schad, P. Belien, G. Verbanck, C.D. Potter, H. Fischer, S.

Lefebvre, M. Bessiere, V.V. Moshchalkov, and Y. Bruynseraede, Phys. Rev. B **57**, 13 692 (1998).

[22] C. Xu, P.M. Hui, and Z.Y. Li, J. Appl. Phys. **90**, 365 (2001).

[23] C.Y. Xiao, J.L. Yang, K.M. Deng, and K.L. Wang, Phys. Rev. B **55**, 3677 (1997).

[24] J.J. Rehr and R.C. Albers, Rev. Mod. Phys. **72**, 621 (2000).

[25] *X-Ray Absorption: Principles, Applications, Techniques of EXAFS, SEXAFS and XANES*, edited by D.C. Koningsberger and R. Prins (Wiley, New York, 1988).

[26] S. Pizzini, F. Baudelet, A. Fontaine, M. Galtier, D. Renard, and C. Marliere, Phys. Rev. B **47**, 8754 (1993).

[27] J.C. Cezar, M.C.M. Alves, D.Z. Cruz, F.C.S. da Silva, M. Knobel, and H. Tolentino, Mater. Sci. Forum **302-303**, 38 (1999).

[28] A.G. Prieto, M.L. Fdez-Gubieda, A. Garcia-Arribas, J.M. Barandiaran, C. Meneghini, and S. Mobilio, J. Magn. Magn. Mater. **221**, 80 (2000).

[29] J.C. Cezar, H.C.N. Tolentino, and M. Knobel, J. Magn. Magn. Mater. **233**, 103 (2001).

[30] P. Allia, P. Tiberto, M. Baricco, and F. Vinai, Rev. Sci. Instrum. **64**, 1053 (1993).

[31] R.H. Yu, X.X. Zhang, J. Tejada, M. Knobel, P. Tiberto, P. Allia, and F. Vinai, J. Magn. Magn. Mater. **164**, 99 (1996).

[32] R.H. Yu, X.X. Zhang, J. Tejada, M. Knobel, P. Tiberto, P. Allia, and F. Vinai, Z. Phys. B: Condens. Matter **99**, 159 (1996).

[33] M.B. Stearns and Y. Cheng, J. Appl. Phys. **75**, 6894 (1994).

[34] H.C.N. Tolentino, A.Y. Ramos, M.C.M. Alves, R.A. Barrea, E. Tamura, J.C. Cezar, and N. Watanabe, J. Synchrotron Radiat. **8**, 1040 (2001).

[35] T. Ressler, J. Synchrotron Radiat. **5**, 118 (1998).

[36] E. Sevillano, H. Meuth, and J.J. Rehr, Phys. Rev. B **20**, 4908 (1979).

[37] W. Bohmer and P. Rabe, J. Phys. C **12**, 2465 (1979).

[38] M. Borowski, J. Phys. IV **7**, C2-259 (1997).

[39] I. Arčon, A. Tuel, A. Kodre, G. Martin, and A. Barbier, J. Synchrotron Radiat. **8**, 575 (2001).

[40] J.P. Renard, P. Beauvillain, C. Dupas, K.L. Dang, P. Veillet, E. Velu, C. Marliere, and D. Renard, J. Magn. Magn. Mater. **115**, L147 (1992).

[41] A. López, F.J. Lázaro, M. Artigas, and A. Larrea, Phys. Rev. B **66**, 174413 (2002).